Presence of Peierls pairing and absence of insulator-to-metal transition in VO2 (A): a structure-property relationship study.

Srinivasa Rao Popuri, Alla Artemenko, Rodolphe Decourt, Antoine Villesuzanne, Michaël Pollet

Presence of Peierls pairing and absence of insulator-to-metal transition in VO_2 (A): A Structure - property relationships study

S. R. Popuri[†‡§], A. Artemenko[†‡], R. Decourt[†‡], A. Villesuzanne[†‡] and M. Pollet[†‡]

[†]CNRS, ICMCB, UPR 9048, F- 33600 Pessac, France

[‡] Univ. Bordeaux, ICMCB, UPR 9048, F-33600 Pessac, France

[§] INCEMC, Plautius Andronescu 1, 300224, Timisoara, Romania

Abstract:

Layered vanadium oxides have been extensively explored due to their interesting metal-insulator transitions and energy conversion/storage applications. In the present study, we have successfully synthesized VO_2 (A) polymorph powder samples by single step hydrothermal synthesis process and consolidated using spark plasma sintering. The structural and electronic properties of the VO_2 (A) were measured over a large temperature range from liquid helium, across the structural transition (400-440 K) and up to 500 K. The structural analysis around this transition reveals an antiferrodistorsive to partially ferrodistorsive ordering upon cooling. It is followed by a progressive antiferromagnetic spin pairing which fully settles at about 150 K. The transport measurements show that, contrariwise to the rutile archetype VO_2 (R/M1), the structural transition comes with a semiconductor to band-type insulator transition. Under these circumstances, we propose a scenario with a high temperature antiferrodistorsive paramagnetic semiconducting phase followed in an intermediate regime with a partially ferrodistorsive paramagnetic semiconducting phase and finally a low temperature partially ferrodistorsive antiferromagnetic band insulator phase with a possible Peierls V-V pairing.

I. Introduction

In spite of the emergence of novel chemically complex oxide materials, compounds with simple binary compositions still surprise us with novel polymorphs and motivate us to understand their structure-property relationships to explore their potentiality for applications.[1-3] Vanadium oxides especially exhibit a wide range of oxidation states, coordination modes, polymorphs and these results in many fascinating

physical phenomena, such as charge and spin ordering, superconductivity, and insulator-metal transitions (IMT).[4-7] Several polymorphs of VO_2, stable at room temperature, have been reported such as the pure M1, A, B, D and N polymorphs or the substituted M2, M3 and M4 phases.[5, 8, 9] Among these polymorphs, except M1, all other polymorphs are either in their synthesis stage or very early stage of understanding their properties and searching for possible applications. In particular, the rutile phase VO_2 (M1) has attracted much attention due to its ultrafast reversible metal-insulator transition near room temperature, promising for applications such as memory switching devices, Mott field-effect transistors, etc.[10-12] The nature of the transition in VO_2 (R/M1) is still under intense debate but all of its degrees of freedom collapse at 340 K.[13] On the other hand, VO_2 (B) shows a multi-phase nature between 4 and 300 K, with a low temperature insulating and magnetically ordered phase, an intermediate temperature insulating phase and a high temperature phase presumably metallic with strong electron correlations.[14] This polymorph also gained a lot of scientific attention due to its layered nature as a cathode material in Li-ion batteries, due to its promising electrochemical properties.[15] VO_2 (A) polymorph was firstly reported by Théobald via a hydrothermal reaction in the V_2O_3-V_2O_5-H_2O system.[16] Several decades later, Oka e al. observed a crystallographic transition between a low temperature phase (LTP, space group P4/ncc, No. 130) and a high temperature phase (HTP, space group I4/m, No. 87) in VO_2 (A) and studied the thermal stability, optical properties and electrical properties on pressed powders.[17] Very recently, this polymorph has been used in cathode, electron emission, and optical switch devices. With low turn-on field and a high field enhancement factor, VO_2 (A) nanobelts are attractive materials for better field emission displays.[18] As cathode material in Li-ion batteries, VO_2 (A) nanostructures also showed a promising capacity of 277 mAh g^{-1}.[19]

We have recently reinvestigated VO_2 (A) crystal structure, the relation between different morphologies and the effect of size/morphology on phase transition temperatures. This led to propose a ‘progressive’ nature for the first-order structural transition.[20] To date, it has been concluded that VO_2 (A) phase goes through a first order structural transition at 440 K, with a doubling of lattice parameter along the c-axis.[21]

The nature of the electronic and insulator-metal phase transitions in VO_2 (A) remains controversial.[22, 23] Very recent study even concluded the tetragonal metallic phase in VO_2(A) around 28–32 GPa.[24] Yet a detailed investigation on the intrinsic electronic transport properties of VO_2 (A) is still lacking, which would help to elucidate the precise nature of the IMT. Further, no information is available on the nature of dominant charge carriers, presence of electron correlations and Debye temperature. The reason for the difficulties in these characterizations lie in the low temperature irreversible phase transition, ca. 773 K, which hinders the densification of samples by conventional sintering methods.[20] One way to overcome this difficulty is to densify the nano- or microscale powder samples under pressure and far below the irreversible phase transition temperature. In this article, we present the electronic transport properties of VO_2 (A) pellets densified using spark plasma sintering (SPS). We also revisit its electrical and magnetic properties, in close relation to structural features.

II. Synthesis and experimental details

In a typical synthesis, V_2O_5 and oxalic acid (OA) are used as reactants; chemicals were of analytical purity and were used without further purification. Initially 0.06 mol/L of V_2O_5 powder was added into 43 mL of deionized water under magnetic stirring for 15 min, followed by adding OA in 1:1.5 ratio to V_2O_5 to form a bright-yellow solution. Then the solution was transferred into the Teflon liner of a stainless steel autoclave. The sealed steel autoclaves were kept in the oven at 250 ^oC for 24 h. After the reaction, the autoclaves slowly cooled down to room temperature (RT). The powders were filtered and washed with distilled water and ethanol to remove unreacted chemical species. In the final step, these powders are dried in air at 80^oC for 6 h, used for further characterizations.

X-ray powder diffraction (P-XRD) patterns of the final products were recorded using a PANalytical X'Pert PRO MPD diffractometer with graphite monochromatic Cu $K_{\alpha 1}$ radiation (λ=1.54178 Å) and were compared with the standards compiled by the Joint Committee on Powder Diffraction and Standards (JCPDS). An Anton-Paar high temperature module of the P-XRD diffractometer was used to study the

reversible phase transition, under vacuum of $9.2x10^{-5}$ bar. The morphology of the products was examined by a field emission scanning electron microscope (FESEM, JEOL JSM - 6300F, 15 kV). The products were deposited on double coated copper conductive tapes and subsequently sputter-coated with a thin layer of gold to prevent charging effects. The samples were compacted isostatically using SPS (SINTER® LAB Series; SPS-511S). Here, VO_2 (A) powders densified under vacuum (10^{-2} mbar) with an applied pressure of 90 MPa. The heating rate up to the sintering temperature was about 100°C/min. Electrical direct current resistivity measurements achieved by the four-probe method with a homemade setup.[25] Low temperature magnetization (at 0.1 T) and specific heat measurements were performed using a Quantum Design MPMS magnetometer and Physical Property Measurement Systems (PPMS), respectively. High temperature magnetization were measurements performed using a Manics DSM 8 type susceptometer under an applied field of 1 T.

III. Results

Morphological studies:

Figure 1 shows the SEM images of the as-obtained powder and the SPS treated powder. The as-obtained powder (Figure 1a) is composed of rectangular micro-rods with lengths ranging from few to several ten micrometres and surfaces ranging from 0.25 to 1 µm². Several trials were made to densify this powder using SPS, varying both the dwell temperature and dwell time. X-ray analysis carried out after the SPS treatments show that the use of temperatures beyond 250°C result in the appearance of the VO_2 (M1) phase. The pellets densified at 250°C for 5 min were used for the transport properties measurements. For such a low sintering temperature, the density of the pellets reaches 71% only, which obviously influences the transport properties. The surface of the pellet prepared by SPS process is shown in Figure 1b; it appears regular with a homogeneous distribution of the porosity.

Structural studies:

The P-XRD patterns of VO_2 (A) measured at room temperature and at 673 K are shown in Figure 2. No secondary phases are visible from these patterns, and the sharp diffraction peaks highlight the high crystalline nature of the sample. A Rietveld refinement was carried out for both patterns using the FullProf package.[26] In addition, a model is refined against the data recorded at 10 K. The results of these analyses are given in Table 1. They are in agreement with our previous report, with the LTP indexed in P4/ncc both at 10 and 300 K and the HTP indexed in I4/m space group.[20] Across the transition, and going to low temperatures, the lattice parameter a decreases about 6% and the lattice parameter c increases about 3%. From 300 K to 10 K, the structure barely evolves: the atomic positions change by less than 5% and the lattice parameters by less than 2%.

The refined cells are sketched in Figure 3. They consist of vanadium tetramer chains aligned along the c-axis and inter-connected in the [110] direction. Within the chains, the oxygen octahedra share edges while they share corners between the chains. The main difference between the HTP and LTP arises from the rotation along the c-axis (along the vanadium chains) of one V-tetrahedron one cell over two, leading to a doubling of the c lattice parameter. The oxygen distribution around the vanadium ions is mostly unaltered with the transition, although the metal-ligand distances slightly evolve and the local symmetry at the cation site, close to C_{4v}, is retained. The vanadium tetrahedra sandwiched between the static ones and the rotating ones strongly distort with a cyclic alternation around the chain direction of short and long distances. On the other hand, the V-V distance perpendicular to the c-axis hardly changes across the transition. The average V-V distance along the chains is 3.082 Å at 673 K while it is 3.06 Å at 300 K with a slight extension for the regular tetrahedron (3.109 Å) and a slight compression for the distorted one (average of 3.011 Å). The data in Table 1 were used to calculate the Madelung potential and its expansion on spherical harmonics, in order to determine the crystal field at each vanadium site and to further get insight in the 3d orbital distribution.[27, 28] For the crystal field calculations, the ratio of the second to the fourth moments of the radial distribution of the 3d electrons ($p = r_0^2\langle r^2\rangle/\langle r^4\rangle$) was set at p=2.[29, 30] The results (angular part only) are sketched in Figure 4. The standard octahedral orbital set (d_{XY}, d_{XZ}, d_{YZ}, d_{X^2-}

$_{Y^2}$, d_{Z^2}) can be used provided that the VO_6^{8-} unit frame is used with the Z-axis directed along the short V-O bond, *i.e.* the direction of a pseudo 4-axis in the nearly C_{4v} environment of the vanadium cation. At 673 K, the orbital distribution is almost ideally described with a Γ^{3+}/Γ^{4-} (E_g/T_{1u}) distortion of the regular octahedron[29]. The d_{Z^2} orbital points toward the closest and the farthest ligand (direction of a pseudo 4-axis; see Figure 3) while the $d_{X^2-Y^2}$ orbital settles perpendicularly, below the basal plan of the distorted octahedron. The d_{XY} and d_{XZ} orbitals alternate along the chain to bridge the vanadium cations and the d_{YZ} orbital bridges the vanadium cations perpendicular to the chains. The departure from C_{4v} is weak and resulted in the splitting of the e_g levels (d_{XZ}, d_{YZ}). With the exception of the d_{YZ} orbital which is invariant upon the Y-Z axis exchange (90° rotation around the X-axis), the ordering is antiferrodistorsive along the chains and between the chains while it is ferrodistorsive perpendicular to the chains. At 300 K, the overall splitting increases, mostly between the e_g levels. In addition, the latter are no longer confined in the XZ and YZ planes and mix. The ordering remains antiferrodistorsive between the chains but is now canted between the levels arising from e_g. Similarly, the ordering remains ferrodistorsive perpendicular to the chains but it is also canted between the e_g levels. Inside the chains, the ordering differs depending on the observed tetramer. For the distorted tetrahedron and along the chain, the ordering is ferrodistorsive along the short V-V bond. It is also ferrodistorsive along the long V-V bond but with only a partial overlap of the orbitals arising from e_g (canted-(anti)ferrodistorsive). In particular, one can notice the strict alignment ($d_{XY}^{V}.d_{XY}^{*V'} = 1$) of the low-lying d_{XY} orbitals centred at the closest vanadium cations. For the second tetrahedron (with equal V-V distances along the chain), the ordering remains globally antiferrodistorsive although it is now canted because of the ferrodistorsive ordering described above. Globally, the main change arises along the chain. At high temperature, the ordering is antiferrodistorsive and the cations bridge through the overlap of d_{XY} and d_{XZ} orbitals. Below the transition temperature, there is a packing of distorted tetrahedra with ferrodistorsive ordering where the cations can bridge through the direct overlap of the low-lying d_{XY} orbitals, and more symmetrical tetrahedra with a canted-antiferrodistorsive ordering,

where the cations bridge through the overlap of the two low-lying orbitals. The same calculations carried out using the P-XRD data at 10 K do not evidence any significant evolution.

Magnetic properties:

The magnetic properties recorded from liquid He temperature to 600 K are shown in Figure 5. Several regimes are visible: (i) below 25 K, the magnetization diverges abruptly; (ii) up to 150 K, it evolves smoothly; (iii) between 400 and 444 K, the large hysteresis signs the structural transition; (iv) in the high temperature limit, above the structural transition temperature (T>444 K), the regime associated with the high temperature phase appears. At low temperature (below 25 K), the magnetization globally follows a Curie-Weiss law (C=0.0071(1) ≈ 2% $S_{1/2}$; θ=-4.9(1) K) with a weak temperature independent contribution of χ_0=6(4)x10^{-6} emu/mole revealing the presence of less than 2% half-spin. The magnetization that persists below 25 K should be interpreted as traces of unpaired spins probably due to defaults in the structure. As the temperature increases, an extended Curie-Weiss regime settles (C=0.0039(6) ≈ 1% $S_{1/2}$; θ=-4(3) K) and the temperature independent contribution χ_0=114(1)x10^{-6} emu/mole) increases significantly. Assuming that these two first contributions are due to impurity centres that exist in the full temperature range and subtracting their contribution (see the corrected magnetization curves in the inset in Figure 5), the high temperature regime can be modelled with a simple Curie-Weiss law (C=0.375(12) = 100% $S_{1/2}$; θ=-127(25) K; χ_0=-30(4)x10^{-6} emu/mole). Both the Curie constant value (matching with the presence of 100% half-spins) and the temperature independent term (perfectly matching the diamagnetic contribution from the ion core) account for the localization of one d^1 electron per vanadium at high temperature. The negative Weiss temperature denotes antiferromagnetic interactions. Below 150 K, the corrected magnetization (inset in Figure 5) drops to zero. From this analysis, it is clear that the HTP is characterized by disordered half-spins sitting at the vanadium sites. Below the transition temperature, the presence of the antiferromagnetic interactions in the HTP and the drop in the magnetization down to 150 K strongly suggest the freezing of the spins with an antiferromagnetic coupling.

Further insight in the magnetic behaviour was obtained from low temperature electron paramagnetic resonance spectroscopy (EPR). The EPR spectra measured as a function of temperature, are shown in Figure 6. Two temperature ranges are clearly visible, i.e. below and above *ca* 165 K. At T= 4 K the spectrum consists of a weakly resolved hyperfine structure superimposed on a very broad (~650 G) resonance line. The set of hyperfine lines originates from isolated V^{4+} ions and is due to dipole–dipole interactions between the unpaired electron moment and the nucleus magnetic moment. The distribution of local crystal field parameters for each unpaired V^{4+} ion (possibly due to their proximity to the surface or to lattice defects such as oxygen vacancies) leads to the hyperfine lines broadening. The lack of well-resolved hyperfine structure of the EPR spectrum hints that V^{4+} ions are located close to each other. This is giving rise to dipole-dipole and magnetic interactions, which resulted in a broad resonance line. As the temperature increases, the hyperfine structure is washed away (becoming fully non-resolved above 60 K) because of the short spin-lattice relaxation time (usual for all d^1 ions). This leads to a strong decrease in the EPR line width from 650 G at 7 K to 180 G at 60 K. Further increase in temperature up to 150 K only leads to the EPR intensity decrease without strong changes in the line width. Above 150 K, both the EPR intensity and the line width change drastically. A hyperfine structure can again be resolved and is superimposed on a broad line alike at liquid helium temperatures (T<30 K). Here the line width increased from 165 G at 150 K to 420 G at 175 K, and the corresponding peak-to-peak intensity also increased from 250 to 680. The inset in Figure 6 shows this change in EPR intensity. A strong increase in the EPR intensity clearly reflects an increase in the density of charged defects at the origin of this resonance. Such non-linear dependence of the EPR line width and intensity with temperature could account, for instance, for spin freezing and/or pairing effects. Between 175-230 K, a plateau in EPR line is observed due to a spectra saturation that arises from additional interactions.

Specific heat studies:

The heat capacity (C_p) data are plotted in Figure 7. The data set can reasonably be modelled using two Debye contributions and a Schottky term. A small deviation appears at low temperature that can be

accounted for using a weak third Debye contribution. The parameters of the fit are given in Table 2. The model departs from the data at *ca* 150 K. The two main contributions to C_p rely on the existence of one oscillator with a low Debye temperature (θ_D≈350 K) and two oscillators with a much higher Debye temperature (θ_D≈850 K). A basic explanation is provided with the presence of a rigid lattice containing two oxygen atoms in the anionic sub-lattice and one vanadium atom in the cationic sub-lattice. The Debye theory gives $\theta_D \propto \sqrt{n/M}$ where n and M stand for the atomic density and mass, respectively. Using n_O=2n_V and M_V≈3M_O, we obtained $\theta_D^V \sim \theta_D^O/\sqrt{6} \sim 825/\sqrt{6} = 337\ K$, which is in fair agreement with the calculated parameters. The Sommerfeld coefficient reveals an enhancement of the effective mass that can be related to a strong interaction of carriers with the lattice, as expected in a Peierls state.[31] In the case of VO_2(M1) to VO_2(R) transition, the entropy change at the transition ranges from 1.6 k_B/vanadium to 3 k_B/vanadium depending on authors, with a large phonon contribution, a small electron contribution and an insignificant magnetic one.[32-34] From differential scanning calorimetry (DSC) measurements the entropy change at the transition in VO_2 (A) is about 0.2 k_B/vanadium.[20, 35] This value is much smaller than in the case of the rutile polymorphs. The linear extrapolation of the excess heat capacity from 150 K to T_t≈440 K (the temperature at the transition on heating) gives an extra $\Delta S \approx 0.7 k_B$/vanadium. This value is very close to $\Delta S \approx k_B \ln(2=2J+1)$, *i.e.* the magnetic entropy expected from the long range ordering of the d^1 electrons. Further entropy changes could also arise from electron interactions, (the Sommerfeld coefficient γ_{HT} in the high temperature phase is missing for an evaluation).

Electrical transport studies:

Oka et al., measured the resistivity of as-pressed pellets of VO_2 (A) powder and observed a rather high resistivity (5×10^3 Ω.cm at 350 K), probably due to the low density of the pellets.[17] The activation energies were 0.8 eV for the LTP-A (below 440 K) and 0.65 eV for the HTP-A (above 440 K). In recent reports on individual nanobelts, an activation energy of 0.28 eV for the LTP-A phase (below 440 K) is reported. Close activation energies of 0.38 eV and 0.33 eV have also been reported for the low and high

temperature phases respectively, from I-V curves on nanowires.[35] Figure 8 shows the evolution of the resistivity between 100 and 500 K (lower temperature data are unavailable because of the apparatus limitation). The overall temperature dependence of the resistivity corresponds to a semiconducting behaviour ($d\rho/dT<0$). This is in agreement with the negligible spectral weight at the Fermi level from X-ray photoelectron spectroscopy measurements.[20] Several regimes are visible, which overall match with the previous observations, and are emphasized on activation energy curves from an Arrhenius-type fit approach $E_a(T) = -k_B \frac{dln(\sigma)}{d(1/T)}$. From 130 K to *ca* 300 K, there is a first regime with a constant activation energy E_a=150 meV, i.e. a value about half the one determined on nanobelts.[3] A jump in E_a(T) at 334-348 K is clearly visible. As noticed earlier, the SPS treatment induces the unavoidable presence of traces of the rutile polymorph and these temperatures are actually characteristic of the M1-R transition. From our DSC measurements and the intensity of the C_p peak at the first transition, the amount of VO_2 (M1) can be estimated and is as less than 5%. At 405-442 K, there is a second jump in E_a and these temperatures correspond to the structural phase transition in VO_2 (A). The activation energy for the carriers in the high temperature phase can be estimated (on cooling only) as 183 meV. These observations rule out the possibility of semiconducting to metallic transition at (or near) the structural phase transition, and rather support a semiconductor-to-semiconductor transition. Our structural data also support this proposition, since the distance between vanadium ions in the HTP-A (3.082 Å) is much higher than both in the metallic VO_2 (R) (2.85 Å) and the Goodenough critical distance for the metallic phase (2.94 Å).[20] The thermopower data is plotted in Figure 9. The negative values over the full range of temperature signs the presence of n-type charge carriers. The high value of the thermopower is consistent with the semiconductor behaviour in both the LTP and HTP. Three transitions are visible at 150, 342 and 426 K matching the ones already observed. The low temperature divergence below *ca* 150 K is characteristic of non-degenerate semiconductors with $\alpha \propto {}^{E_g}/_{T}$ and discards an activation of the mobility (E_g=634 meV).

Such abrupt increase of the thermopower can be related to a rapid decrease of the density of charge carriers. The absolute value of the thermopower slowly decreases in the intermediate temperature regime

from 150 K to 426 K; the jump at 342 K signs the presence of (M1) and/or (R) polymorphs. The second jump at 426 K marks the LTP-HTP structural transition.

IV. Discussion

The transition at *ca* 340 K is due to the emergence of traces of the rutile polymorph (VO_2 (M1/R)) during the sintering process. There is indeed no evidence for the presence of VO_2 (M1/R) in the P-XRD measurements up to 673 K (Figure 2), the magnetic measurements (Figure 5) and EPR experiments (Figure 6) carried out on the powders prior the sintering. Its signature is however very clear from the transport measurements with abrupt jumps at 342 K in the thermopower (Figure 9), and 334 K and 348 K in the activation energy (Figure 8) on cooling and heating cycles, respectively. Comparison with previous reports allows estimating the amount of VO_2(R/M1) impurities to be less than 5%. Below 160 K, the set of hyperfine lines visible from EPR originates from isolated V^{4+} ions and the presence of localized carriers as seen from macroscopic magnetic measurements are due to defects, probably at the surface of the sample. All the remaining features are considered intrinsic to the VO_2 (A) polymorph and three distinct regimes can be described (Table 3).

The high temperature phase, i.e. above 426 K from thermopower measurements (Figure 9) consists in a pseudo-uniaxial structure (I4/m) with a tetrameric packing of edge-sharing VO_6^{8-} octahedra, aligned along the c-axis to form packed chains of vanadium tetrahedra and these chains link through octahedral corner sharing (Figure 3). Within the chains, the vanadium-vanadium distance is constant at 3.082 Å and far above the Goodenough critical distance for the metallic phase (2.94 Å). The symmetry remains quite high (C_{4v}-like with a weak lifting of the e_g doublet degeneracy) and the orbital layout is antiferrodistorsive along the chains. The transport measurements are characteristic of an n-type semiconductor with a high resistivity decreasing as the temperature increases (activation energy of 183 meV) and a high value of the Seebeck coefficient, ranging from -75 to -20 µV/K from 426 to 500 K. This HTP is paramagnetic with antiferromagnetic interactions and our results account for one unpaired electron (S=1/2) per vanadium as expected from the composition. When the temperature decreases (below 426 K from thermopower

measurements), one over two vanadium tetrahedron rotates leading to the doubling of the cell along the c-axis (P4/ncc). This affects the V-V distances along the chains which remain constant (*ca* 3.1 Å) in one tetrahedron over two, but shorten (2.769 Å) vs. lengthen (3.253 Å) in the other one. This modifies the orbital layout with, in particular, a global ferrodistorsive ordering along the chains in the distorted tetrahedron (the ordering in the other one remains antiferrodistorsive). This structural and orbital transition is associated with a first jump in the properties. There is a progressive freezing of the magnetization, which completes at *ca.* 150 K, signing a slow antiferromagnetic ordering. It is visible from EPR experiments with the appearance of new lines from 160 K, and the saturation as the temperature increases when the number of unpaired vanadium ions increases. It is also visible from heat capacity measurements with an entropy excess between 150 K and 440 K estimated at $\Delta S \approx 0.7 k_B$/vanadium, *i.e.* $\Delta S \approx k_B \ln(2=2J+1)$ with J=1/2, matching the entropy release expected from the breaking of spin pairs. The transport properties are also changing with a raise in both the resistivity and the thermopower. The nature of the dominant carriers remains unaltered and the activation energy decreases to 150 meV. Below 150 K, the structure barely evolves, only a decrease in the cell volume was observed and the orbital layout remains the same. The heat capacity results account for an ideal rigid structure and the magnetization drops to zero as the antiferromagnetic ordering completes. The electric conductivity drops but the main change lies in the thermopower that collapses, signing an abrupt reduction of the density of charge carriers, which could be assigned to the pairing of vanadium ions.

From these analyses, we propose for VO_2 (A) a scenario in temperature with essentially two breakdowns. At high temperature (*ca* 440 K), a first order structural transition associated with the emergence of a partial ferrodistorsive ordering and a low temperature (*ca* 150 K) Peierls-like transition with the pairing of vanadium cations once the freezing of the spins in antiferromagnetic singlets completes. In essence, this behaviour is quite close to the one of the archetype VO_2 (R/M1) polymorphs. However, while all the degrees of freedom collapse at the same temperature in VO_2 (R/M1), it happens sequentially in VO_2 (A) and the change in the properties is much less sharp. Among the possible explanations, one can think of the absence of a metallic phase at high temperature and the lack of sufficiently strong electron correlations as

proposed for the VO_2 (R/M1) polymorph. In addition, the structural transition in VO_2 (R/M1) is based on some breathing of the linear chains, the structure of VO_2 (A) is more constrained and the transition is more complex with a cooperative rotation of the vanadium tetrahedra. From these comments, the behaviour of VO_2 (A) actually appears intermediate between the one of VO_2 (R/M1) and the one of VO_2 (B).[14]

V. Conclusions

We have synthesized VO_2 (A) powder samples by single step hydrothermal synthesis and consolidated these powders using low temperature and high-pressure spark plasma sintering process. Based on structural, electrical, thermal and magnetic properties, we propose a three-regimes and two-step scenario to explain the transitions of VO_2 (A) with temperature. At high temperature (*ca* 440 K), there is a first order structural transition involving a cooperative rotation of the vanadium tetrahedra, associated with the emergence of a partial ferrodistorsive ordering. At low temperature (*ca* 150 K), a Peierls-like transition occurs with the pairing of vanadium cations along with the freezing of the spins in antiferromagnetic singlets. In contrast with VO_2 (M1), both the sequential transitions and the constrained structure lead to less pronounced changes in the properties across the transitions as highlighted by the semiconductor nature of the compound on its whole temperature existence domain.

Acknowledgments

S.R.P., A.V., M.P. and A.A. gratefully acknowledge financial support from European Community's Marie Curie Initial Training Network (ITN) 7th Framework Programme - SOPRANO FP7/ 2007-2013 (Grant Agreement No. 214040) and European Community's Marie Curie Incoming International Fellowship (IIF) 7th Framework Programme - EPREXINA FP7/2007-2013 (Grant Agreement No. 255662) respectively. S.R.P gratefully acknowledge the assistance of I. Bucur (INCEMC), M. Miclau (INCEMC), A. Brull (ICMCB), S. Gomez (ICMCB), O. Nguyen (ICMCB) and S. Fourcade (ICMCB) during the synthesis and characterizations.

Tables:

Table 1. Rietveld refinements results of LTP-A (at 10 and 300 K) and HTP-A phases. Some characteristic distances are given bottom of the table.

Table 2. Parameters used to model the heat capacity data of VO_2 (A).

Table 3. Synopsis of results and analyses (FD: ferrodistorsive; AFD: antiferrodistorsive; PM: paramagnetic; AFM: antiferromagnetic; HFS: hyperfine structure; SC: semiconductor with activation energy mentioned when available).

Figures:

Figure 1. SEM morphology overview images of (a) as-synthesized VO_2 (A) micro-rod crystals prepared using hydrothermal process at 523 K for 24 h and (b) cross-sectional overview of a pellet obtained by SPS with 523 K - 90 MPa conditions.

Figure 2. Powder X-ray diffraction patterns measured at 300 K (a) and 673 K (b). Red dots: experimental data; black lines: model; green vertical lines: Bragg peak positions; blue line: difference curve between data and model. The 'wine' coloured tick markers are from sample holder.

Figure 3. Sketch of VO_2 (A) cells at 300 K and 673 K. The atomic positions at 673 K are shifted by (¼ ¼ 0) for easier comparison. For each temperature, a first half of the cell (left) highlights the octahedral environment and the tetramer packing, while the second half (right) highlights the vanadium tetrahedra sequence. The view at 673 K also shows the rotation of a vanadium tetrahedron one cell over two that leads to the doubling of the cell in the low temperature phase and the shortening/lengthening of some V-V distances along the chain. The colouring of the bonds highlights their sequence in the chain (green: short; blue: intermediate; orange: long). On the right side and for each temperature, a sketch of the oxygen environment of the vanadium ion with the metal-ligand distances and top views of the chains are given; the rotation of the tetrahedron at 673 K is also illustrated.

Figure 4. 3d orbital distribution at the vanadium sites at 673 K (left) and at 300 K (right). Each orbital is named after the main contribution (almost ideal) and relative to the (X, Y, Z) molecular frame sketched in the cells, the Z axis being along the direction of the shortest V-O bond for each VO_6^{8-} unit. The relative energies of the five d orbitals are also drawn.

Figure 5. Temperature variation of the magnetic susceptibility (M/H) of VO_2 (A) measured below and above room temperature. 1: heating cycle after zero magnetic field cooling; 2: cooling cycle after heating

under magnetic field; 3: heating cycle under magnetic field; 4: cooling cycle under magnetic field. Inset: same data corrected for extrinsic features (see text).

Figure 6. Electron resonance spectra of VO_2 (A) between 7 K and 280 K. Frames in the legend are highlighting the two regimes observed. The high temperature spectra are also marked with dots (at about 3350 G) for visibility. Inset: EPR intensity as a function of temperature.

Figure 7. Low temperature heat capacity measurements. Circles: experimental data; red lines: model (see text and Table 2); the red dashed curve shows the difference (x10) between the data and the model; the green dotted line approximates the difference, used to evaluate the excess entropy (see text).

Figure 8. Resistivity as a function of temperature during heating (red circles) and cooling cycles (blue circles). The dashed lines (arb. units) show the evolution of the activation energy from an Arrhenius-type fit.

Figure 9. Thermopower as a function of temperature. The jump at 300 K is artificial and is due to the different setups for the low and high temperature measurements.

	LTP-VO_2 (A)		HTP-VO_2 (A)
T (K)	10	300	673
Space group	P4/ncc (130)	P4/ncc (130)	I 4/m (87)
a (Å)	8.42074 (9)	8.43478 (4)	8.4819 (3)
c (Å)	7.67303 (10)	7.67220 (4)	3.8257 (2)
Z	16	16	8
Atomic positions			
x_V	0.4486 (1)	0.4484 (1)	0.3000 (5)
y_V	0.7237 (1)	0.7243 (1)	0.0242 (6)
z_V	0.1302 (2)	0.1296 (1)	0
x_{O1}	0.4078 (3)	0.4055 (1)	0.5018 (2)
y_{O1}	0.7481 (3)	0.7481 (2)	0.1588 (1)
z_{O1}	0.3781 (8)	0.3765 (7)	0
x_{O2}	0.4085 (3)	0.4102 (2)	0.1622 (4)
y_{O2}	0.4099 (3)	0.4098 (2)	0.157 (2)
z_{O2}	0.3743 (9)	0.3727 (8)	0
Vanadium-Vanadium distances along the chains (Å)			
Short	2.755(1)	2.769(2)	
Middle	3.112(1)	3.109(1)	3.082(1)
Long	3.248(2)	3.253(1)	
Vanadium-Vanadium distances perpendicular to chains (Å)			
Intra-chain	3.373(1)	3.380(1)	3.418(2)
Inter-chains	3.603(2)	3.617(1)	3.610(2)

Table 1.

Debye 1		Debye 2		Debye 3	
N	Θ_D (K)	N	Θ_D (K)	N	Θ_D (K)
0.97	359	2	825	0.03	108
γ (mJ/mole.K^2)		Schottky			
		Δ_1 (K)		n	
6.83		3.4		0.0038	

Table 2.

Temperature → / Properties ↓	150 K	426 K	
Crystal structure	P4/ncc Distortion and Vanadium-Vanadium bonds shortening ; Partially FD		I4/m AFD
C_p	Rigid ionic frame Light electron correlations	Excess entropy matching $k_B.\ln(2.½+1)$	
Magnetic	AFM	Spins freezing	PM
	Defects traces		
EPR	Unpaired spins (HFS) Interacting spins (broad line)	Increase of unpaired spins (reappearance of HFS up to saturation) Loss of interactions	
Thermopower	Intrinsic SC (band insulator) 634 meV	SC	SC
Resistivity	SC	SC (150 meV)	SC (183 meV)
Summary	Partially FD AFM band insulator with possible Peierls pairing	Partially FD SC with AFM interacting spins	AFD PM SC

Table. 3:

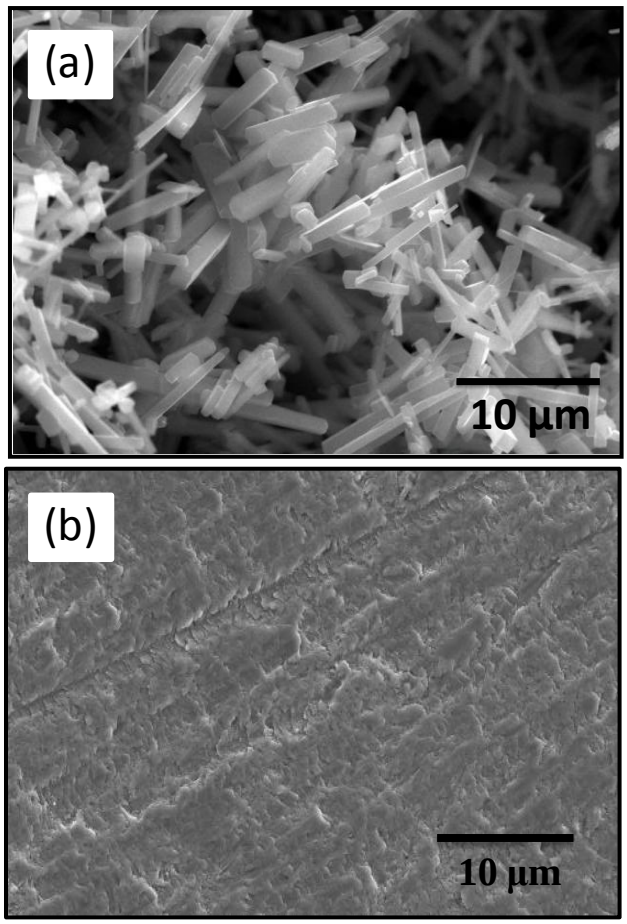

Figure 1.

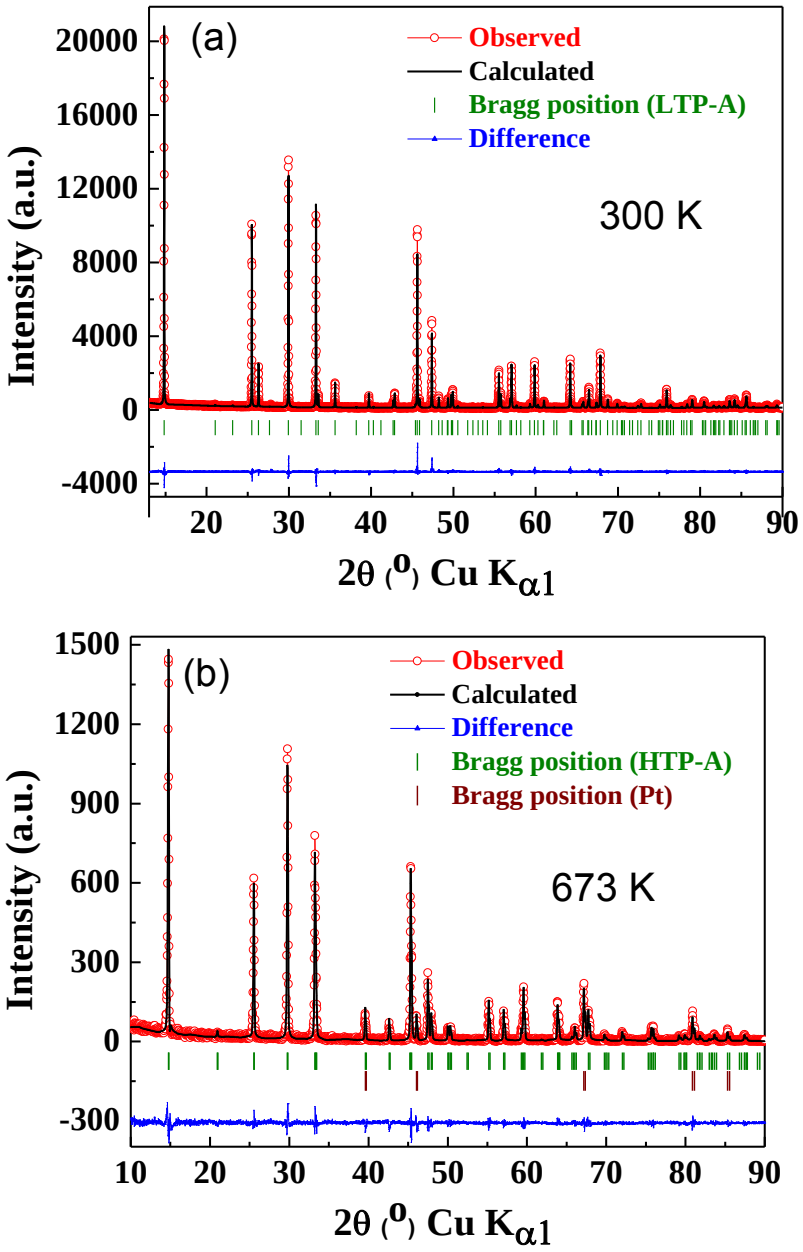
(a)
Observed
Calculated
Bragg position (LTP-A)
Difference
300 K
Intensity (a.u.)
20000
16000
12000
8000
4000
0
-4000
20
30
40
50
60
70
80
90
2θ (⁰) Cu Kα1
(b)
Observed
Calculated
Difference
Bragg position (HTP-A)
Bragg position (Pt)
673 K
Intensity (a.u.)
1500
1200
900
600
300
0
-300
10
20
30
40
50
60
70
80
90
2θ (⁰) Cu Kα1

Figure 2.

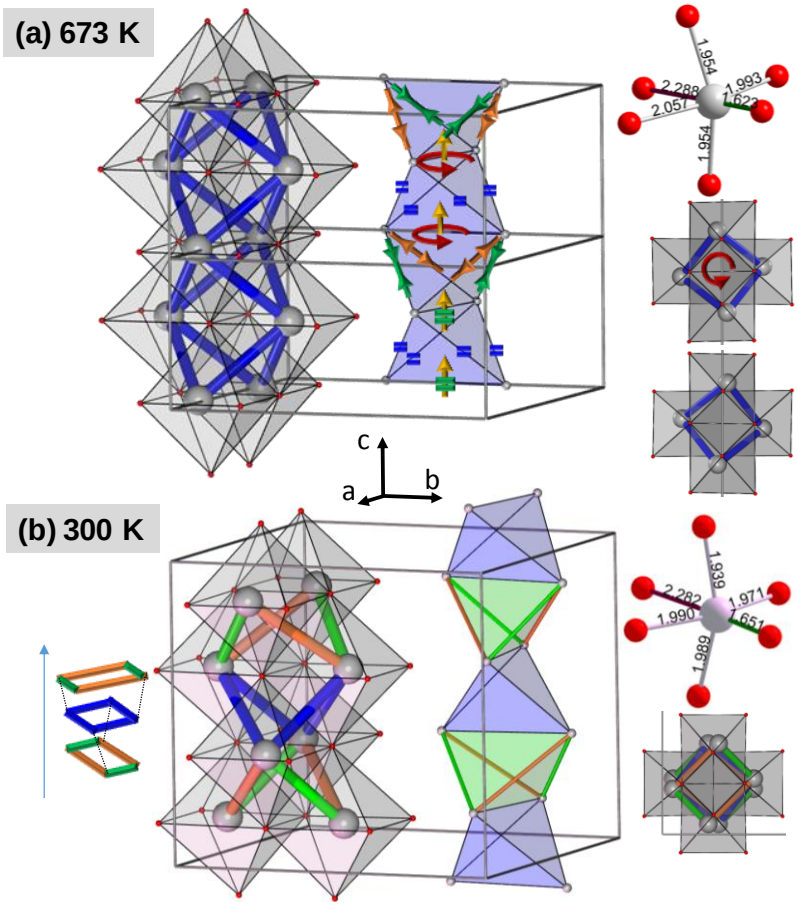
(a) 673 K
1.954
2.288
1.993
2.057
1.622
1.954
c
a
b
(b) 300 K
1.939
2.282
1.971
1.990
1.651
1.989

Figure 3.

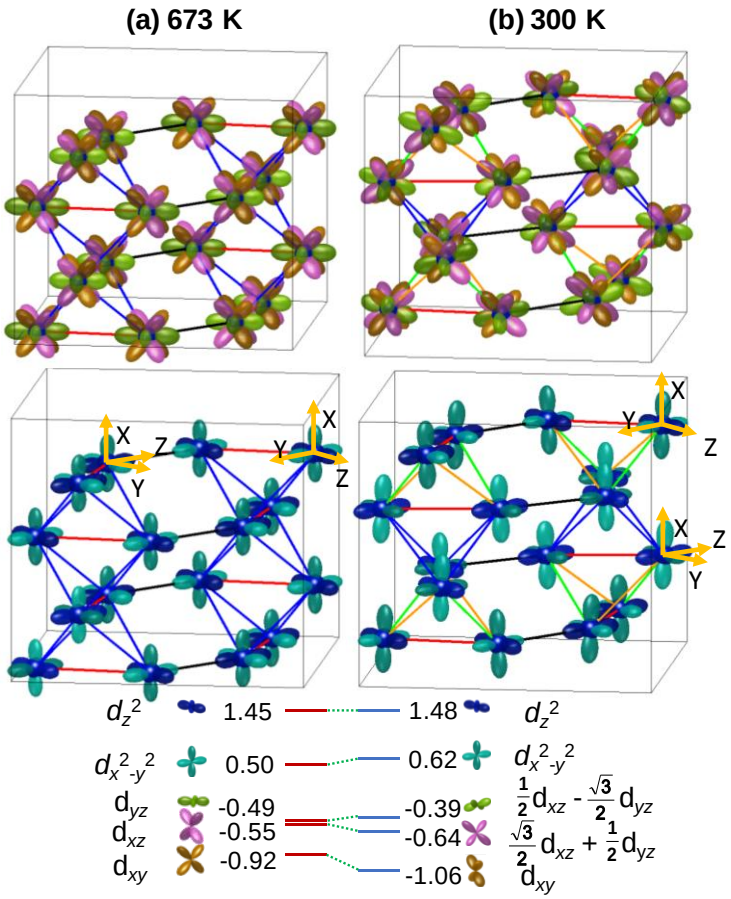
(a) 673 K
(b) 300 K
X
Y
Z
d_{z^2}
1.45
1.48
d_{z^2}
$d_{x^2-y^2}$
0.50
0.62
$d_{x^2-y^2}$
d_{yz}
d_{xz}
d_{xy}
-0.49
-0.55
-0.92
-0.39
-0.64
-1.06
$\frac{1}{2}d_{xz} - \frac{\sqrt{3}}{2}d_{yz}$
$\frac{\sqrt{3}}{2}d_{xz} + \frac{1}{2}d_{yz}$
d_{xy}

Figure 4.

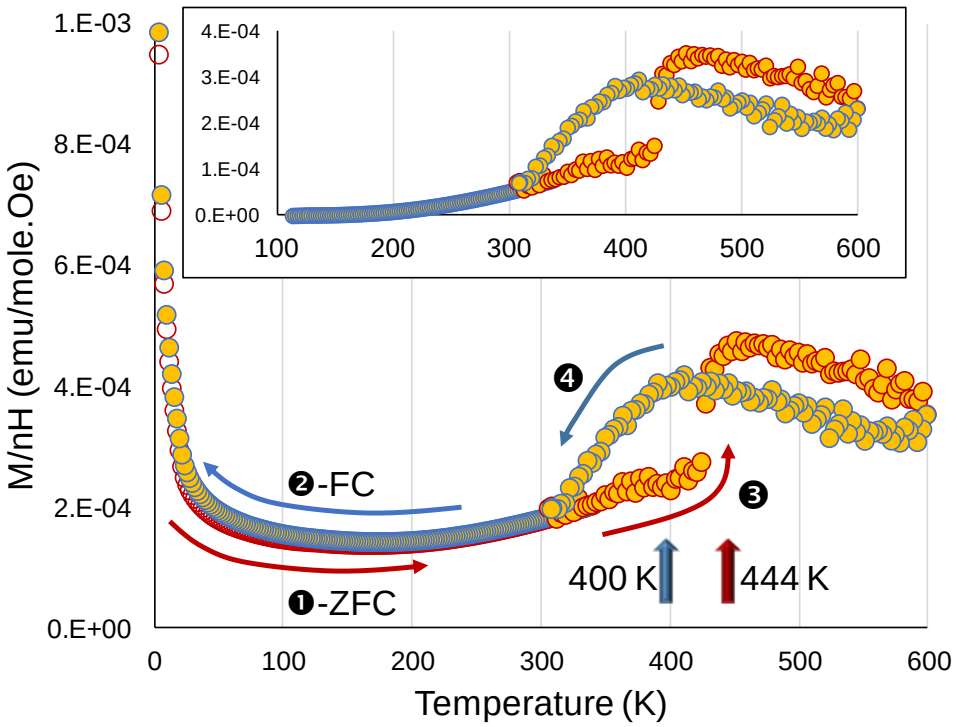
1.E-03
8.E-04
6.E-04
4.E-04
2.E-04
0.E+00
M/nH (emu/mole.Oe)
0
100
200
300
400
500
600
Temperature (K)
4.E-04
3.E-04
2.E-04
1.E-04
0.E+00
100
200
300
400
500
600
❹
❷-FC
❸
❶-ZFC
400 K
444 K

Figure 5.

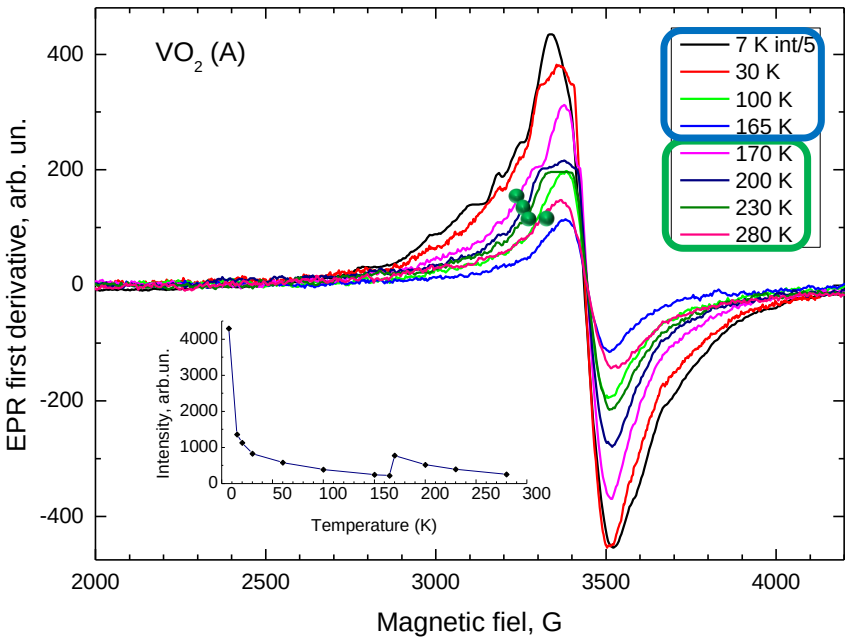
VO2 (A)
7 K int/5
30 K
100 K
165 K
170 K
200 K
230 K
280 K
EPR first derivative, arb. un.
Magnetic fiel, G
Intensity, arb.un.
Temperature (K)

Figure 6.

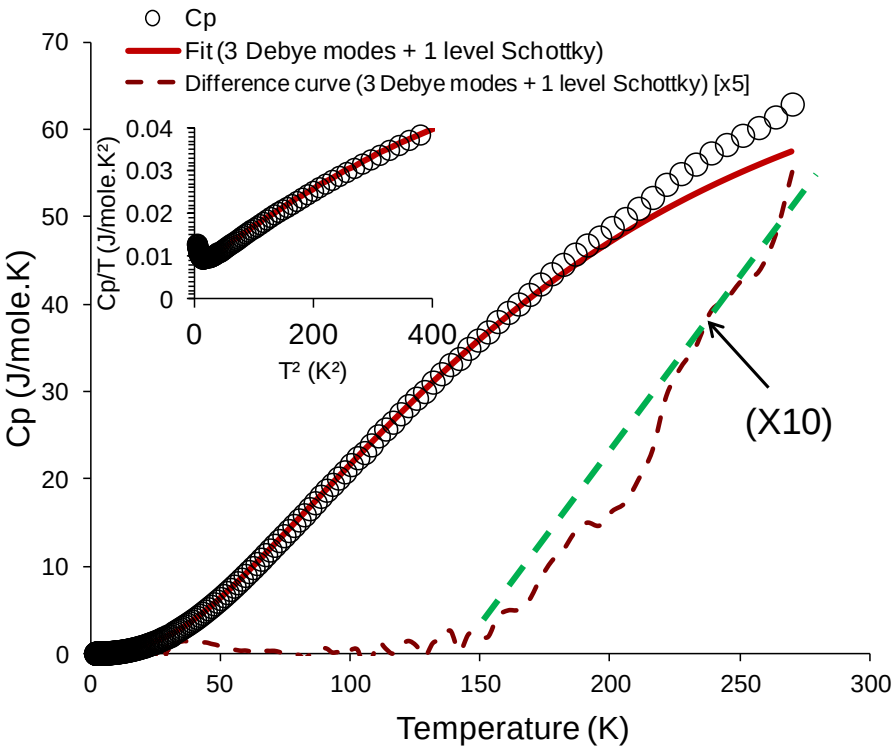
Cp
Fit (3 Debye modes + 1 level Schottky)
Difference curve (3 Debye modes + 1 level Schottky) [x5]
Cp (J/mole.K)
Temperature (K)
Cp/T (J/mole.K²)
T² (K²)
(X10)

Figure 7.

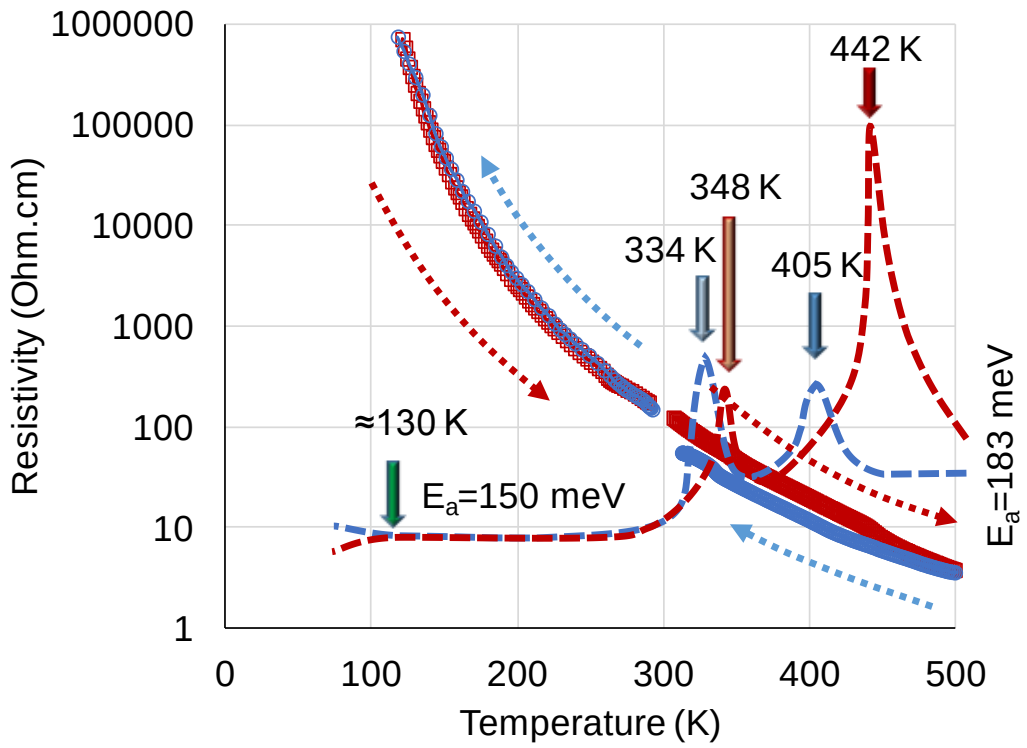
1000000
100000
10000
1000
100
10
1
Resistivity (Ohm.cm)
0
100
200
300
400
500
Temperature (K)
442 K
348 K
334 K
405 K
≈130 K
Ea=150 meV
Ea=183 meV

Figure 8.

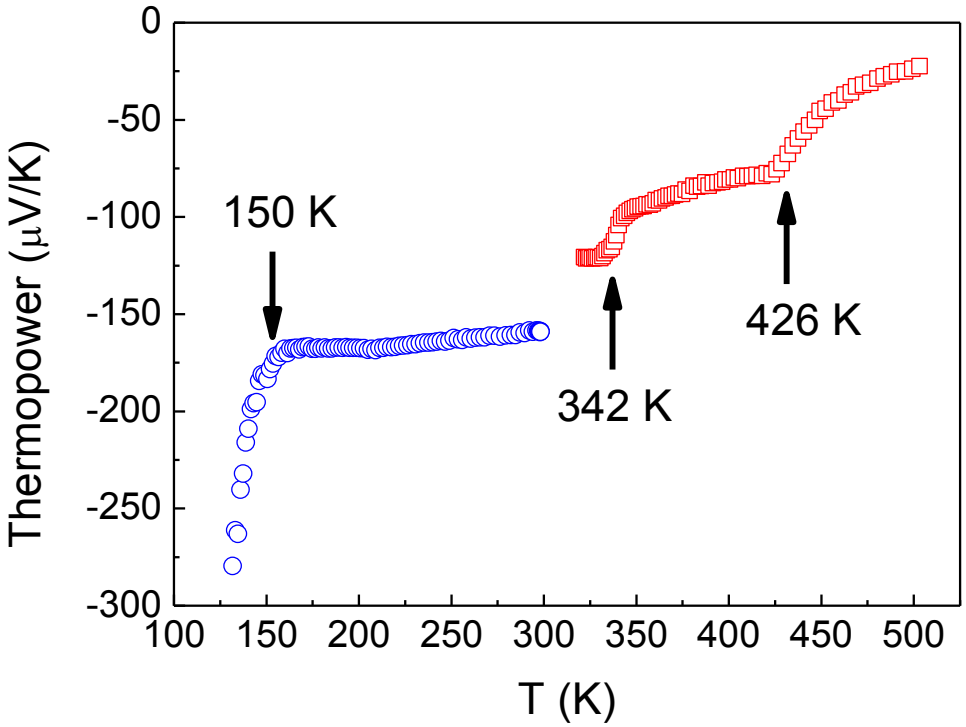
0
-50
-100
-150
-200
-250
-300
Thermopower (μV/K)
150 K
342 K
426 K
100
150
200
250
300
350
400
450
500
T (K)

Figure 9.

VI. References

1. T. Zhu and S.-P. Gao, *The Journal of Physical Chemistry C*, 2014, **118**, 11385-11396.
2. D. Weber, A. Stork, S. Nakhal, C. Wessel, C. Reimann, W. Hermes, A. Müller, T. Ressler, R. Pöttgen and T. Bredow, *Inorganic chemistry*, 2011, **50**, 6762-6766.
3. C. Wu, H. Wei, B. Ning, J. Yang and Y. Xie, *Chemical Communications*, 2010, **46**, 1845-1847.
4. N. A. Chernova, M. Roppolo, A. C. Dillon and M. S. Whittingham, *Journal of Materials Chemistry*, 2009, **19**, 2526-2552.
5. V. Eyert, *arXiv preprint cond-mat/0210558*, 2002.
6. T. Yamauchi, M. Isobe and Y. Ueda, *Solid state sciences*, 2005, **7**, 874-881.
7. J. Yamaura, T. Yamauchi, E. Ninomiya, H. Sawa, M. Isobe, H. Yamada and Y. Ueda, *Journal of magnetism and magnetic materials*, 2004, **272**, 438-439.
8. S. R. Popuri, M. Miclau, A. Artemenko, C. Labrugere, A. Villesuzanne and M. l. Pollet, *Inorganic chemistry*, 2013, **52**, 4780-4785.
9. L. Bai, Q. Li, S. A. Corr, Y. Meng, C. Park, S. V. Sinogeikin, C. Ko, J. Wu and G. Shen, *Physical Review B*, 2015, **91**, 104110.
10. F. Morin, *Physical Review Letters*, 1959, **3**, 34.
11. E. Strelcov, Y. Lilach and A. Kolmakov, *Nano letters*, 2009, **9**, 2322-2326.
12. H.-T. Kim, B.-G. Chae, D.-H. Youn, S.-L. Maeng, G. Kim, K.-Y. Kang and Y.-S. Lim, *New Journal of Physics*, 2004, **6**, 52.
13. H.-T. Kim, Y. W. Lee, B.-J. Kim, B.-G. Chae, S. J. Yun, K.-Y. Kang, K.-J. Han, K.-J. Yee and Y.-S. Lim, *Physical review letters*, 2006, **97**, 266401.
14. S. R. Popuri, A. Artemenko, R. Decourt, M. Josse, U.-C. Chung, D. Michau, M. Maglione, A. Villesuzanne and M. Pollet, *The Journal of Physical Chemistry C*, 2015, **119**, 25085-25092.
15. C. Nethravathi, C. R. Rajamathi, M. Rajamathi, U. K. Gautam, X. Wang, D. Golberg and Y. Bando, *ACS applied materials & interfaces*, 2013, **5**, 2708-2714.
16. F. Théobald, *Journal of the Less Common Metals*, 1977, **53**, 55-71.
17. Y. Oka, T. Ohtani, N. Yamamoto and T. Takada, *Nippon seramikkusu kyokai gakujutsu ronbunshi*, 1989, **97**, 1134-1137.
18. M. Li, F. Kong, L. Li, Y. Zhang, L. Chen, W. Yan and G. Li, *Dalton Transactions*, 2011, **40**, 10961-10965.
19. L. Dai, Y. Gao, C. Cao, Z. Chen, H. Luo, M. Kanehira, J. Jin and Y. Liu, *RSC Advances*, 2012, **2**, 5265-5270.
20. S. R. Popuri, A. Artemenko, C. Labrugere, M. Miclau, A. Villesuzanne and M. Pollet, *Journal of Solid State Chemistry*, 2014, **213**, 79-86.
21. Y. Oka, S. Sato, T. Yao and N. Yamamoto, *Journal of Solid State Chemistry*, 1998, **141**, 594-598.
22. S. Zhang, B. Shang, J. Yang, W. Yan, S. Wei and Y. Xie, *Physical Chemistry Chemical Physics*, 2011, **13**, 15873-15881.
23. C. Wang, J. Shao, X. Liu, Y. Chen, W. Xiong, X. Zhang and Y. Zheng, *Physical Chemistry Chemical Physics*, 2016, **18**, 10262-10269.
24. B. Cheng, Q. Li, H. Zhang, R. Liu, B. Liu, Z. Yao, T. Cui, J. Liu, Z. Liu and B. Sundqvist, *Physical Review B*, 2016, **93**, 184109.
25. P. Dordor, E. Marquestaut and G. Villeneuve, *Revue de Physique Appliquée*, 1980, **15**, 1607-1612.
26. J. Rodríguez-Carvajal, *Physica B: Condensed Matter*, 1993, **192**, 55-69.
27. B. Nijboer and F. De Wette, *Physica*, 1957, **23**, 309-321.
28. F. De Wette and B. Nijboer, *Physica*, 1958, **24**, 1105-1118.
29. M. Pollet and A. Artemenko, *The Journal of Physical Chemistry A*, 2013, **117**, 6536-6547.
30. R. Gallay, J. Van der Klink and J. Moser, *Physical Review B*, 1986, **34**, 3060.
31. P. Cox, Clarendon Press, Oxford, 1992.

32. A. Zylbersztejn and N. F. Mott, *Physical Review B*, 1975, **11**, 4383.
33. J. H. Park, J. M. Coy, T. S. Kasirga, C. Huang, Z. Fei, S. Hunter and D. H. Cobden, *Nature*, 2013, **500**, 431-434.
34. J. D. Budai, J. Hong, M. E. Manley, E. D. Specht, C. W. Li, J. Z. Tischler, D. L. Abernathy, A. H. Said, B. M. Leu and L. A. Boatner, *Nature*, 2014, **515**, 535-539.
35. C. Wang, X. Liu, J. Shao, W. Xiong, W. Ma and Y. Zheng, *RSC Advances*, 2014, **4**, 64021-64026.